

Structure and magnetism of Fe-Co alloy nanoparticles

Z. Klencsár^{1,*}, P. Németh¹, Z. Sándor¹, T. Horváth¹, I.E. Sajó², S. Mészáros³, J. Mantilla⁴, J.A.H. Coaquira⁴, V.K. Garg⁴, E. Kuzmann⁵, Gy. Tolnai¹

¹*Institute of Materials and Environmental Chemistry, Research Centre for Natural Sciences, Hungarian Academy of Sciences, Magyar tudósok körútja 2, 1117 Budapest, Hungary;*

²*University of Pécs, Szentágotthai Research Centre, Pécs, H-7624, Ifjúság str. 20, Hungary;*

³*Institute of Nuclear Research of the Hungarian Academy of Sciences, Bem tér 18/c, Debrecen 4026, Hungary;*

⁴*Institute of Physics, University of Brasilia, 70919 - 970 Brasilia, DF, Brazil;*

⁵*Institute of Chemistry, Eötvös Loránd University, Pázmány P. s. 1/A, 1117 Budapest, Hungary;*

Abstract

We report the hydrothermal synthesis and structure of Fe_xCo_{1-x} alloy nanoparticles with considerable stability against oxidation under ambient atmosphere. Powder X-ray diffractometry (XRD), transmission electron microscopy (TEM), energy dispersive X-ray spectroscopy (EDX), inductively coupled plasma mass spectrometry (ICP-MS), ⁵⁷Fe Mössbauer spectroscopy and magnetization measurements are applied to characterize the composition, morphology, crystal structure, atomic order and magnetic properties of the nanoparticles. As-prepared samples are composed mainly of the bcc Fe_xCo_{1-x} alloy phase. TEM images of heat-treated samples confirm the nanoparticle nature of the original alloys. A consistent analysis of the experimental results leads to $x \approx 53\%$ and $x \approx 62\%$ Fe atomic ratio respectively in two analogous alloy samples, and suggests that the atomic level structure of the nanoparticles corresponds to that of a fully disordered (A2-type) alloy phase. Exploration of the effect of cobalt on the ⁵⁷Fe hyperfine parameters of iron microenvironments suggests that in these alloys the electronic state of Fe atoms is perturbed equally and in an additive manner by atoms in their first two coordination spheres.

Keywords: nanoparticles; disordered alloys; hyperfine interactions; Mössbauer spectroscopy

*Corresponding author, e-mail: klencsar.zoltan@ttk.mta.hu

1. INTRODUCTION

The Fe-Co binary alloy system is widely studied on account of its advantageous soft magnetic properties such as highest levels of saturation magnetization, high permeability, low magnetocrystalline anisotropy and high Curie temperature [1], as well as of its catalytic activity [2,3]. Several investigations of $\text{Fe}_x\text{Co}_{1-x}$ alloys have been initiated by the peculiar non-monotonic functional dependence of the average magnetic moment on the x composition parameter [4,5,6], as well as by the ability of the system to form with different degrees of (B2-type, see, e.g. [7]) atomic order for the same composition [5,8,9,10]. Hyperfine interaction parameters (such as the hyperfine magnetic field at the iron nuclei and the ^{57}Fe isomer shift) measured by ^{57}Fe Mössbauer spectroscopy have been found to be especially well suited to reflect changes in the magnetic and electronic state of iron atoms as a function of Co concentration and of the degree of disorder in $\text{Fe}_x\text{Co}_{1-x}$ alloys [5,6,8,9].

On account of their high saturation magnetization and associated high magnetophoretic mobility, in the form of nanoparticles Fe-Co alloys are considered as promising candidates for the realization of advanced biological and biomedical functions such as highly specified biological in vitro cell separations [11], therapeutic (hyperthermia treatment [12] and drug delivery [13]) and diagnostic (magnetic contrast agents in magnetic resonance imaging [14]) applications. Their use is also considered as advantageous in industrial magnetic heating applications, for example in the form of solder-nanoparticle composites that enable localized reflow soldering by the use of AC magnetic fields [15].

Various preparation methods, such as mechanical alloying [16], polyol [17,18,19] and sol-gel [20,21] process, transmetallation [22], coprecipitation [23], as well as co-reduction [24] with ultrasound assistance [25] have been reported to result in Fe-Co alloy nanoparticles with various Co concentration levels. Due to their large reactive specific surface area, fine metal powders can be susceptible to spontaneous ignition under exposure to air, and consequently they require special precautions regarding their storage and manipulations [26]. Particularly, iron nanoparticles with a characteristic size in the order of ~ 100 nm are known to be already pyrophoric [27]. Thus, from the point of view of their applicability, long-term stability against oxidation under ambient conditions is an important desirable feature of metallic and

alloy nanoparticles. For the case of Fe-Co alloys, sol-gel and polyol processes were recently reported to lead to air-stable nanoparticles [19,21].

The degree of atomic order/disorder in the body centered cubic (bcc) crystal lattice of Fe-Co alloys influences their magnetic and mechanical properties [1,6,9,10,28], and are therefore also considered as an important characteristic of Fe-Co alloy nanoparticles. The degree of disorder is also reflected in the mean ^{57}Fe hyperfine magnetic field and ^{57}Fe isomer shift Mössbauer parameters of $\text{Fe}_x\text{Co}_{1-x}$ alloys [6,8,9], which provides a possible way to explore atomic disorder in Fe-Co alloy nanoparticles via ^{57}Fe Mössbauer spectroscopy. Following [29,30] and successive related works [28,31], it may be possible to derive information on the degree of disorder and the Co concentration in a single step by fitting the ^{57}Fe Mössbauer spectrum of $\text{Fe}_x\text{Co}_{1-x}$ alloy nanoparticles on the basis of a corresponding microscopic model that (I) enumerates the various individual Fe microenvironments by considering the possible local atomic arrangements of Co and Fe atoms in the first few atomic shells around a particular central Fe atom, and (II) assumes that the effects of neighboring atoms are additive concerning the ^{57}Fe isomer shift and ^{57}Fe hyperfine magnetic field detected at the central Fe atom irrespective of their relative location with respect to each other.

Though this approach was adopted and successfully applied for dilute alloys [29,30], the validity of its use for a wider composition range including non-dilute alloys may be seen as questionable. On the one hand because below $\sim 730^\circ\text{C}$ the equiatomic FeCo system favors the B2 ordered structure (with Fe and Co being positioned exclusively at the cube corners and the cube centers of the bcc lattice, respectively) [1] suggesting that the formation of nearest neighbor (n.n.) Co-Fe atom pairs is energetically favorable with respect to that of n.n. Co-Co pairs [30], which may prevent the formation of a fully disordered (A2-type [7]) atomic structure for compositions where the appearance of Co-Co n.n. pairs should have appreciable probability. On the other, because the mentioned additive effects of neighboring atoms are expected to show a dependence on the magnetic moment of Fe atoms and thus on the Co concentration [6].

Nevertheless, for disordered $\text{Fe}_x\text{Co}_{1-x}$ alloys the dependence of the mean ^{57}Fe hyperfine magnetic field on the Co concentration was successfully described in a rather wide (34-70 at.% Co) concentration range by assuming the additivity of the hyperfine field perturbation effects of Co/Fe atoms situated in the first two nearest neighbor shells of Fe

atoms [31]. Furthermore, in equiatomic FeCo alloys the effect of disorder on the mean ^{57}Fe hyperfine magnetic field was also successfully modeled on the same ground [28].

In the present work we report the successful preparation and structural as well as magnetic characterization of $\text{Fe}_x\text{Co}_{1-x}$ alloy nanoparticles displaying considerable stability against oxidation under ambient atmosphere, with emphasis on the assessment of their composition and atomic order/disorder characteristics.

2. EXPERIMENTAL

2.1. Synthesis

Fe-Co alloy nanoparticles were synthesized from iron(III) chloride hexahydrate and cobalt(II) acetate (both from Sigma-Aldrich, reagent grade quality) as precursors and aluminium powder (average size: 100 micron) and ammonium fluoride (from Sigma-Aldrich, “Puriss $\geq 98\%$ ”) applied as reducing materials. Aqueous solutions were made from double distilled water purified with Milli-Q systems. The synthesis of nanoparticles was carried out as follows. 10 mmol cobalt(II) acetate and 7.5 or 10 mmol (depending on sample) iron(III) chloride hexahydrate were dissolved separately, each in a separate volume of 90 cm^3 distilled water. After dissolution the iron(III) chloride solution was added to the cobalt(II) acetate solution under vigorous stirring. 120 mmol ammonium fluoride dissolved in 40 cm^3 distilled water were then added to the solution immediately. The fluoride solution thus obtained was stirred continuously for 15 minutes, which step was followed by the addition of 20 mmol aluminum powder. This mixture was stirred for another 15 minutes and was heated to 80°C with heating rate of 2°C/minutes. It was then maintained at this temperature for 60 minutes. The steel-gray colored iron/cobalt product was collected from the bottom of the reactor magnetically by a strong permanent magnet and washed three times with deionized water and finally with ethanol. It was then dried at 40°C for 4 hours in vacuum and stored in closed glass bottles.

Following their preparation, the samples thus obtained, referred to as S1 and S2, were handled under ambient atmosphere. Portions of the samples S1 and S2 were heat treated at 650°C for 4 hours under ambient air and cooled down to ambient temperature in several hours. These heat treated samples will be denoted in the followings as DS1 and DS2, respectively.

2.2. Characterization

Transmission electron microscopy (TEM) and scanning electron microscopy (SEM) measurements were carried out on the DS1 and DS2 samples by a Morgagni 268D (operating at 100 kV) and a Zeiss EVO40 (operating at 20 kV) instrument, respectively. Chemical measurements were performed using an Oxford INCA energy dispersive X-ray (EDX) spectrometer at 20 kV. The Fe:Co atomic ratio was determined by taking into account the corresponding calibration measurements performed on known mixtures of Fe₂O₃ and Co₂O₃. We identified the calibration curve (Figure S1) and developed the following equation for estimating the true Fe/(Fe+Co) ratio (y) in our samples:

$$y = 0.848q^2 + 0.164q, \quad (1)$$

where q denotes the measured Fe/(Fe+Co) ratio.

Composition of the alloy nanoparticles was measured by the means of inductively coupled plasma mass spectrometry (ICP-MS) performed with a Thermo Scientific “iCAP Qc” spectrometer. KED (kinetic energy discrimination) mode was applied with He as single collisional gas to decrease the spectral interferences caused by the formation of polyatomic (molecular) ions in the plasma. The samples S1 and S2 were first dissolved by using nitric acid and hydrochloric acid solutions, and then were further diluted with distilled water to concentration levels below 1 mg/L for Fe and Co. The dissolved sample mass was 54.6 mg and 51.2 mg in the case of S1 and S2, respectively.

X-ray powder diffraction (XRPD) patterns of the as-prepared Fe-Co alloy powders were obtained at room temperature with a Philips PW3710 based PW1050 Bragg-Brentano parafocusing goniometer by using Cu K_α radiation, graphite monochromator and proportional counter. The scattering angle 2θ was adjusted in the range of 35...105 deg in step scan mode with a step size of 0.04 deg and a counting time of 1 s per step. The lattice parameters and the characteristic crystallite size of the nanoparticles were determined by fitting the diffraction peaks to Lorentzian functions with position and full width at half maximum (FWHM) parameters determined on the basis of Bragg’s law and Scherrer’s equation [32], respectively, the latter being used in the form of

$$\Gamma_+(2\theta)/\text{deg} = \frac{180}{\pi} \frac{0.9\lambda}{d \cos \theta}, \quad \Gamma(2\theta) = \Gamma_0 + \Gamma_+(2\theta) \quad (2)$$

where d is the characteristic size (diameter) of the crystallites, $\lambda \approx 0.154186$ nm is the wave length of the applied Cu K_α radiation, $\Gamma(2\theta)$ denotes the full width (FWHM) of the diffraction peak associated with the scattering angle 2θ , and $\Gamma_0 = 0.11$ deg accounts for instrumental broadening.

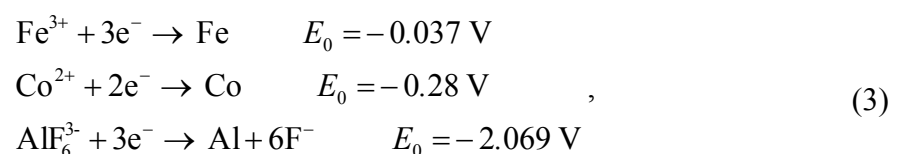
Magnetic measurements were performed by the means of a Quantum Design SQUID magnetometer. High-field magnetization measurements were carried out up to external magnetic fields of 90 kOe on ~ 35.8 mg of sample S2 at 300 K as well as at 5 K. FC-ZFC magnetization measurements were carried out on the same sample in the temperature range of 5...300 K by applying a driving field of ~ 118 Oe.

^{57}Fe Mössbauer spectra of the S1 and S2 powders were recorded in transmission geometry by using $^{57}\text{Co}(\text{Rh})$ radioactive sources and conventional spectrometers (Wissel and KFKI) operated in constant acceleration mode. Different Mössbauer spectrometer setups were used to measure spectra at room temperature and at ~ 80 K. A Mössbauer cryostat (Janis) applying cooling with liquid nitrogen vapor was applied in the latter case. ^{57}Fe isomer shift (δ) values are given relative to that of α -iron at room temperature. The spectra were analyzed by assuming the nuclear gyromagnetic factors of $g_e = -0.103267$ and $g_g = +0.18088$ for the excited ($I_e = 3/2$) and ground ($I_g = 1/2$) state of the ^{57}Fe nucleus.

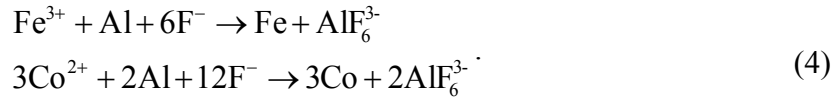
^{57}Fe Mössbauer spectra and X-ray diffractograms were analyzed by using version 4.0Pre of the MossWinn program [33] that was complemented with auxiliary libraries providing the fitting functions accounting for the XRPD measurements and for the binomial distribution of Fe/Co atoms in the cubic lattice of the studied alloys [34] as described in the text.

3. RESULTS AND DISCUSSION

In aqueous solutions containing different metal cations (i.e. Fe^{3+} and Co^{2+}) along with metallic particles (i.e. Al), the driving force for the reduction process is the difference between the standard reduction potentials (E_0). The corresponding potential values in the case of our system are [35]



with the reduction processes being



Due to its low standard electrode potential ($E_0 = -1.662$ V [35]) finely dispersed metallic aluminum exhibits significant reducing power, and can therefore be applied for wet-chemical redox synthesis of both metallic and non-metallic elements [36]. This strong reducing capability is further enhanced by the presence of fluoride ions in the solution, as in this case the electrode potential is even lower ($E_0 = -2.069$ V). This increase in the difference between the electrode potentials is of great importance from the point of view of the reaction rate of redox chemical reactions. Due to the relatively small difference between the standard electrode potentials of the two metal cations in our system, their reduction will take place close to the same rate. This phenomenon allows the formation of an alloy as opposed to separately reduced single-metal particles.

The X-ray powder diffractograms of the as-prepared Fe-Co alloy samples S1 and S2 are displayed in Figure 1. The discernable reflections can all be indexed according to a body-centered cubic (bcc) crystal lattice, which confirms the successful formation of the $\alpha\text{-Fe}_x\text{Co}_{1-x}$ alloy phase, and suggests that the as-prepared samples are not sensitive to oxidation under ambient conditions. The (111) superlattice reflection (at $2\theta \approx 55.9$ deg)—that could indicate ordering [1,10]—is not observed, though on account of the small difference between the X-ray scattering factors of Fe and Co atoms, at the applied X-ray energy (~ 8041 eV for Cu K_α radiation) the relative intensity of the (111) reflection should be very low even if ordering was present [1,10]. The broadening of the individual peaks can be fairly described by Scherrer's equation (2). The cubic lattice parameter and the characteristic crystallite size obtained for S1 and S2 by fitting of the corresponding diffractograms (Figure 1) are listed in Table 1. The cubic lattice parameter of $\text{Fe}_x\text{Co}_{1-x}$ is known to decrease with increasing Co concentration in bulk samples [1,4,37] as well as in micron- [38] and ~ 100 nm [39] sized particles. Determination of the Co concentration in our samples on the basis of the comparison of the observed lattice parameters (Table 1) with the above quoted results [1,4,37,38,39] could, however, lead to an overestimation of the Co concentration. Namely, even though the cubic lattice parameter observed for Fe-Co particles with a characteristic size in the order of ~ 100 nm agrees fairly well with that observed for corresponding bulk samples [39], for particles with a size below a few times of 10 nm decreasing particle size is expected

to lead to an increase in the magnitude of surface-stress related lattice strain effects and thereby to a reduction of the lattice parameter [40,41]. The peculiar behavior of Fe-Co alloy nanoparticles is furthermore underlined by the recent finding of an *increasing* {001} crystal-plane distance with increasing Co concentration in $\text{Fe}_x\text{Co}_{1-x}$ nanoparticles with a size in the order of ~ 10 nm [25]. In order to avoid ambiguity related to the above effects, in this work we base the determination of the composition of the Fe-Co alloy nanoparticles on the combination of results provided by the methods of EDX, ICP-MS and ^{57}Fe Mössbauer spectroscopy.

Figure 2 and Figure 3 show TEM images of the heat treated DS1 and DS2 samples. They show the abundant presence of near isodiametric particles with a characteristic size in the order of ~ 10 -20 nm, and that of strongly anisometric nanoparticles with a length in the order of ~ 100 nm but with a much smaller characteristic width of only ~ 5 -10 nm. On the basis of the corresponding selected area electron diffraction (SAED) patterns, the observed features can be identified as (Co,Fe)O having the rock salt structure. As the applied heat treatment is unlikely to promote the formation of nanoparticles, these images must reflect the morphology of the original S1 and S2 samples, and thereby confirm the nanoparticle nature of the original Fe-Co alloy. We note that in addition to (Co,Fe)O, in the heat treated samples DS1 and DS2 further phases with a crystal structure akin to that of hematite and magnetite could also be identified (see, e.g., Figures S2 and S3).

The X-ray diffractograms of the original alloy samples did not show appreciable dependence of the reflection peak broadening on the lattice plane of reflection (Figure 1), which suggests that the XRD reflections are mainly due to the nearly isodiametric nanoparticles. The original samples can therefore be seen as being composed mainly from isodiametric Fe-Co alloy nanoparticles.

Figure 4 displays mass magnetization measurements performed on sample S2 at 5 K as well as at 300 K. The shape of the $M(H)$ curve is typical for a soft magnetic material, whereas the order of magnitude of the observed rather high saturation magnetization of $M_{s,5\text{K}} \approx 206$ emu/g is characteristic of Fe-Co alloys (see, e.g., [22,23,42,43]). The reduction of M_s with respect to the bulk saturation magnetization value (~ 240 emu/g) is expected to be caused mainly by the presence of a magnetically dead, low-magnetization surface layer of the nanoparticles [44]. The change of saturation magnetization from 5 K to 300 K

($M_{s,300K} \approx 200$ emu/g) is minimal in accordance with the high Curie temperature of Fe-Co alloys [39].

Figure 5 shows the results of ZFC-FC magnetization measurements of sample S2. The ZFC and FC curves display a moderate divergence with decreasing temperature starting at the blocking temperature of $T_b \approx 215$ K. The divergence appears due to particles whose magnetic moments are blocked along the local magnetic anisotropy axes at temperatures below T_b , while being prone to thermal agitation at higher temperatures. The blocking temperature found for S2 is lower than that observed for carbon-coated Fe-Co nanoparticles with an average particle size of ~ 7 nm [43] or 20-30 nm [45], suggesting the presence of particles with a lower level of magnetic anisotropy energy barrier in our sample. Nevertheless, the blocking effect remains moderate in magnitude until the lowest temperatures applied. The low-temperature limit of the M_{ZFC}/M_{FC} magnetization ratio (R_0) appears to be enhanced by interparticle magnetic interactions, as illustrated by FC-ZFC magnetization measurements carried out on Fe-Co nanoparticles being either in close contact ($R_0 \approx 0.88$) [23], or carbon coated ($R_0 \approx 0.64$) [43,45] or dispersed in polyvinylpyrrolidone ($R_0 \approx 0.13$) [46] in order to increase interparticle distances. In our case $R_0(S2) \approx 0.96$ suggesting that our sample behaves as a collection of mostly strongly interacting magnetic particles, where the observed blocking effect is presumably associated with the smallest, least interacting particles.

The Fe:Co atomic ratios measured by the EDX spectrometer for samples DS1 and DS2 (see Figures S4 and S5) are listed in Table 2 together with the corresponding corrected values calculated on the basis of the calibration curve's equation (Eq. (1), Figure S1). The deviation is significant, which points to the importance of the EDX calibration procedure in the determination of the proper Fe:Co ratio of Fe-Co alloys. The corrected results are in excellent agreement with the results of ICP-MS measurements of the original S1 and S2 alloy samples (Table 3). Thus, sample S1 is a nearly equiatomic alloy, whereas S2 contains a moderate excess of iron with respect to cobalt. Taking this into account, the lattice parameters obtained for S1 and S2 (Table 1) are below that of the corresponding bulk alloys [47] by ca. 0.14%, which could be due to a size-dependent lattice strain effect [41].

With respect to the concentration ratios of Fe and Co atoms in the initial solution, an increased iron concentration is present in the resulting alloy particles. With respect to cobalt,

this enrichment in iron is expected on account of the higher probability of iron ions to become reduced in the solution due to their higher standard reduction potential.

^{57}Fe Mössbauer spectra of samples S1 and S2 measured at room temperature ($T \approx 293\text{ K}$) and at $T \approx 80\text{ K}$ are shown in Figure 6. The main contribution to the spectra comes from a magnetic sextet component that can be associated with the Fe-Co alloy phase. A minor doublet component appears in the spectra at both temperatures with a relative spectral area contribution of $\sim 5\%$ (at 293 K, decreasing to 3-4% at 80 K), and parameters of $\delta = 0.36(3)\text{ mm/s}$, $\Delta = 0.98(4)\text{ mm/s}$ and $\Gamma = 0.80(7)\text{ mm/s}$ (at 293 K), which can be associated with paramagnetic or superparamagnetic FeOOH particles, on the basis of the above parameters presumably mainly with $\beta\text{-FeOOH}$, apparently being a minor side product of the applied preparation procedure. The relatively low amount and a possibly low crystallinity of this iron(III) oxide-hydroxide component [48] may prevent the appearance of corresponding reflections to become discernable in the X-ray diffractograms of Figure 1, but may in part have also contributed to the reduction of the observed specific saturation magnetization value (Figure 4).

The presence of this additional iron containing phase in our samples means that the iron concentration in the Fe-Co alloy phase may be smaller than that derived on the basis of EDX (Table 2) and ICP-MS (Table 3) measurements. Taking this possibility into account, the numbers given for iron in Table 2 and Table 3 should be reduced by ~ 2 , resulting in roughly 1% decrease in the iron concentration of the alloy phase, bringing the corresponding compositions closer to 50:50 and 60:40 in samples S1 and S2, respectively. At the same time, similar amounts of additional Co bearing phases (whose amount is too low to be detected in our XRPD measurements) may also occur in our samples, which may partly or wholly compensate for the above effect on the Fe:Co ratio. For this reason, in the followings we consider the Fe:Co ratios given in Table 2 and Table 3 without the above correction.

The mean ^{57}Fe hyperfine parameters characterizing the Fe-Co alloy phase are straightforwardly derived by fitting the corresponding subspectrum to a single sextet envelope. The spectrum of disordered Fe-Co alloys are known to show a characteristic asymmetry of the six absorption peaks [31] due to the presence of numerous different iron microenvironments and a corresponding distribution in the hyperfine parameters such as the ^{57}Fe hyperfine magnetic field and isomer shift. As a consequence, an accurate fit of the

spectra on Figure 6 requires the assumption of independent amplitudes and line widths for all the six peaks. In addition, each of the six peaks can be expected to be the sum of numerous close-centered overlapping Lorentzians associated with the individual microenvironments. This is expected to lead to a Gaussian broadening of the individual peaks, transforming their shape from Lorentzians (Figure S6) towards Voigt line profiles [49]. In accordance with this expectation, we found that fitting the peaks of the sextet with pseudo-Voigt [49] line profiles—characterized by the same Lorentzian width and different Gaussian broadenings—yields a fit (see Figures S7 and S8) that is considerably improved with respect to that carried out by the use of Lorentzian line profiles (see Figure S6), corroborating the presence of atomic disorder in our samples. The Fe-Co alloys’ mean hyperfine parameters resulting from these fits are given in Table 4. Comparing the observed mean B_{hf} and δ parameters with the Co concentration dependence of corresponding data obtained for bulk samples [5,6,8,31], we find that the mean parameters given in Table 4 are in accordance with the Fe:Co atomic ratios listed in Table 2 and Table 3. In particular, in the studied concentration range the higher mean hyperfine magnetic fields observed for sample S2 with respect to that of S1 is in agreement with the higher Fe concentration in the alloy phase of S2. In addition, on the basis of the mean hyperfine parameters we can also characterize our samples concerning their atomic order [5,6,8,31]. On the basis of the mean isomer shift values (Table 4) observed at ~ 293 K (compare with [8]) and ~ 80 K (compare with [6]) both S1 and S2 can be classified as having a disordered atomic structure. The mean hyperfine magnetic field values observed in our samples at $T \approx 80$ K are in fair agreement with this conclusion [6]. At the same time, the $B_{\text{hf,m}}$ (293 K) values appear to be lower (roughly by ~ 0.5 T, see [8]) than expected for a disordered structure alloy with the present compositions (Table 2 and Table 3). Such hyperfine magnetic field reduction may also be the result of thermal excitation of the nanoparticles’ magnetic moment [50], which effect should be more pronounced for particles with smaller dimensions. As the data of Table 1 shows, sample S1 has the lower characteristic crystallite size, and thus we hypothesize the magnetic moment of its Fe-Co particles to be more susceptible to thermal excitations than in the case of sample S2. This hypothesis appears to be confirmed by the temperature dependence of the mean hyperfine magnetic field (Table 4), which is more pronounced in the case of sample S1. Namely, the decrease in the value of $B_{\text{hf,m}}$ as the temperature changes from 80 K to 293 K is

roughly twice as large in the case of S1 (~ 0.95 T) than in the case of S2 (~ 0.48 T). Note that in contrast with our finding regarding the present nanoparticle samples, in bulk samples the temperature dependence of the mean ^{57}Fe hyperfine magnetic field was found to become *weaker* with increasing Co concentration [51]. This can be seen as a further indication for the role of the small particle size and the associated collective magnetic excitations in determining the value of $B_{\text{hf},m}$ at room temperature in the present samples.

A standard way of detailed analysis of ^{57}Fe Mössbauer spectra of Fe-Co alloys is the derivation of the corresponding hyperfine magnetic field distributions with the implicit assumption that the isomer shift depends linearly on the hyperfine magnetic field [6,28,31,51]. In order to facilitate comparison with associated works, we have carried out a similar analysis of our spectra, the corresponding results being included in the Supplement (see Table S1 and Figures S9 and S10). In the followings, however, we proceed along a more direct and constrained way of analysis, by considering the effect of the number of Co/Fe atoms in the first two shells around a particular central Fe atom on the associated hyperfine parameters, similarly to methods described in [28,29,30]. In the bcc structure the first two atomic shells of an Fe atom is composed of 8 nearest neighbor (n.n.) and 6 next nearest neighbor (n.n.n.) atoms. We assume that the effects of n.n. and n.n.n. Fe atoms on the hyperfine magnetic field, isomer shift and quadrupole shift characterizing the central Fe atom are additive, and do not depend on their relative location. The actual model that we have applied enabled the consideration of different effect magnitudes for n.n. and n.n.n. atoms, as well as of different preferences/probabilities of atoms for taking the α (bcc cube corner) and β (bcc cube center) sites of the cubic structure as put forward in [28]. In this approach the hyperfine parameters of a sextet spectrum component associated with an iron atom with $N_{\text{nn}} = 0 \dots 8$ n.n. Fe atoms and $N_{\text{nnn}} = 0 \dots 6$ n.n.n. Fe atoms are expressed as

$$\begin{aligned}
 B_{\text{hf}}(N_{\text{nn}}, N_{\text{nnn}}) &= B_{\text{hf},0} + N_{\text{nn}} \cdot \Delta B_{\text{hf},\text{nn}} + N_{\text{nnn}} \cdot \Delta B_{\text{hf},\text{nnn}} \\
 \delta(N_{\text{nn}}, N_{\text{nnn}}) &= \delta_0 + N_{\text{nn}} \cdot \Delta \delta_{\text{nn}} + N_{\text{nnn}} \cdot \Delta \delta_{\text{nnn}} \\
 2\varepsilon(N_{\text{nn}}, N_{\text{nnn}}) &= 2\varepsilon_0 + N_{\text{nn}} \cdot \Delta 2\varepsilon_{\text{nn}} + N_{\text{nnn}} \cdot \Delta 2\varepsilon_{\text{nnn}}
 \end{aligned} \tag{5}$$

where $B_{\text{hf},0} \equiv B_{\text{hf}}(0,0)$ is the hypothetical hyperfine magnetic field expected for an iron atom around which the first two atomic shells contain Co atoms only, whereas $\Delta B_{\text{hf},\text{nn}}$ and $\Delta B_{\text{hf},\text{nnn}}$ are the increase in the hyperfine magnetic field as a result of an additional Fe atom in the first and in the second atomic shell, respectively, with analogous meanings of corresponding

parameters regarding δ and 2ε . The $w(c_{\text{Fe}}, p_\alpha, p_\beta, N_{\text{nn}}, N_{\text{nnn}})$ probability of occurrence (and thus the relative spectral weight) of the altogether 63 sextet components were calculated as given in [28], where c_{Fe} denotes the concentration of iron in the alloy, whereas p_α and p_β denote respectively the proportion of α and β sites of the cubic structure that are occupied by Fe atoms. (For a fully disordered system $c_{\text{Fe}} = p_\alpha = p_\beta$, whereas for perfect B2-type order we have $c_{\text{Fe}} = 0.5$, $p_\alpha = 1$ and $p_\beta = 0$.)

Due to the relatively small effect a single n.n. or n.n.n. Fe atom has on the hyperfine parameters of the central iron atom, the individual peaks of the ^{57}Fe Mössbauer spectra of Fe-Co alloys are—apart from their broadening—rather feature-poor (see for example Figure 6 or [6,28]). As a consequence, the application of the above model in its most general form can turn out to be unfeasible unless additional constraints are applied to reduce correlations among the fit model parameters. As a main constraint, we have assumed that at room temperature all fit parameters appearing in Eq. (5) are the same for samples S1 and S2, and fitted the corresponding two spectra accordingly, with a simultaneously adjusted parameter set. Though this constraint disregards the predicted dependence of the additive perturbation parameters ($\Delta B_{\text{hf,nn}}$, $\Delta B_{\text{hf,nnn}}$, etc.) on the cobalt concentration of the alloy [6], for the concentration range spanned by our samples (Table 2, Table 3) we expect this dependence to be mild. Namely, the concentration dependence of perturbation parameters is expected to follow from that of the iron magnetic moment, which latter changes only moderately around Co concentrations of 40-50% in disordered alloys [6]. On the other hand, a model based on constant perturbation parameters was already found to describe the experimental data satisfactorily in the Co concentration range of 34...70 at.% [31].

With this constraint set, we aimed at finding a corresponding solution where c_{Fe} , treated as a fit parameter, converged to the predicted values (Table 2, Table 3) for both S1 and S2. Remarkably, such solution was found only when the applied model was considerably simplified with the following constraints:

$$\begin{aligned}
 \Delta B_{\text{hf,nn}} &= \Delta B_{\text{hf,nnn}} \\
 \Delta \delta_{\text{nn}} &= \Delta \delta_{\text{nnn}} \\
 \Delta 2\varepsilon_{\text{nn}} &= \Delta 2\varepsilon_{\text{nnn}} \\
 c_{\text{Fe}} &= p_\alpha (= p_\beta)
 \end{aligned}
 \tag{6}$$

meaning that the effects of n.n. and n.n.n. iron atoms are treated as identical (being—for the sake of brevity—in the followings denoted with ΔB_{hf} , $\Delta\delta$ and $\Delta 2\varepsilon$), and the alloy is assumed to be fully disordered. In addition, strong correlation found between δ_0 and $\Delta\delta$ prevented the independent determination of these parameters, so we fixed $\Delta\delta$ to +0.0025 mm/s, in accordance with a corresponding value reported earlier [31].

The parameters we have obtained in the above way from the fit of the room temperature ^{57}Fe Mössbauer spectra of samples S1 and S2 (Figure 6) are listed in Table 5. There is an excellent agreement between the obtained c_{Fe} iron concentration values and the Fe:Co ratio determined with EDX (Table 2) and ICP-MS measurements (Table 3). The obtained isomer shift and quadrupole shift values are both in a reasonable range for the number of n.n. and n.n.n. iron neighbors that have appreciable probability to occur for the given concentration levels (i.e. for $N_{\text{nn}}+N_{\text{nnn}} = 3\dots 12$). The values of $B_{\text{hf},0} \approx 28.7$ T and $\Delta B_{\text{hf}} \approx 0.77$ T compare well with corresponding values of bulk disordered alloy samples ($B_{\text{hf},0} \approx 30.2$ T, $\Delta B_{\text{hf},\text{nn}} \approx 0.72$ T and $\Delta B_{\text{hf},\text{nnn}} \approx 0.66$ T) [31]. The smaller $B_{\text{hf},0}$ value observed in our case may be connected to the higher ΔB_{hf} value we obtained in the frame of our more constrained model, but may also be contributed to by collective magnetic excitations associated with the nanosized nature of the present samples. The difference between the applied iron surface densities of the measured Mössbauer samples of S1 and S2 being negligible (in the order of 1%), the moderate (~ 0.03 mm/s) difference between the line widths of the individual Lorentzians making up the sextets of the model fitted for S1 ($\Gamma \approx 0.29$ mm/s) and S2 ($\Gamma \approx 0.26$ mm/s) may refer to the influence of the 3rd and further atomic shells on the hyperfine magnetic field at the central iron atom. Namely, the higher line width obtained for sample S1 can be rationalized by considering that the corresponding c_{Fe} iron concentration is closer to 50% where the variance of binomial distribution takes on its maximum, which situation is expected to lead to the largest line broadening as caused by the corresponding distribution of the cumulative magnitude of additional hyperfine magnetic fields contributed to the B_{hf} at the central iron atom by 3rd and further atomic shells.

The successful description of our Mössbauer spectrum data on the basis of the assumption of equal perturbations of the ^{57}Fe hyperfine magnetic field due to n.n. and n.n.n. iron atoms harmonizes with the conclusion put forward concerning $\text{Fe}_{0.99}\text{Co}_{0.01}$ [52] where Co atoms were found to cause close to equal perturbation of the hyperfine magnetic field at n.n. and

n.n.n. Fe sites by nuclear-magnetic-resonance techniques. Though the magnitude and direction of change in B_{hf} due to a single Co (n.n. or n.n.n.) neighbor reported in [52] is different from that observed by us, this is expected on account of the dependence of the corresponding perturbation effects on the Co concentration [6].

The ^{57}Fe Mössbauer spectra measured at $T \approx 80$ K were fitted with a model similar to that applied for the fit of the spectra measured at room temperature, but with the c_{Fe} iron concentration being fixed to the values obtained from the fit of the room-temperature spectra. The parameters obtained in this way are listed in Table 5 whereas the spectrum fits are displayed in Figure 6. The fit required the assumption of different $B_{\text{hf},0}$ values for S1 and S2, $B_{\text{hf},0}$ for S2 being somewhat reduced with respect to that of S1, which may be connected to the tendency of the mean iron magnetic moment to increase with increasing Co concentration [6]. With respect to sample S1, the larger mean ^{57}Fe hyperfine magnetic field found for sample S2 at 80 K (Table 4) will then follow from the larger probability of occurrence of iron in the first two coordination spheres of iron atoms.

The difference between the line widths obtained at $T \approx 80$ K is the same as that at room temperature within the error of the fit (Table 5), whereas the larger overall line widths at $T \approx 80$ K can be due to a larger experimental line broadening resulting from the different Mössbauer setup applied for the low-temperature measurements.

It is remarkable that ΔB_{hf} observed at ~ 80 K and ~ 293 K match within error, suggesting that the perturbative effect of neighboring atoms on the magnetic state of the central Fe atom does not depend appreciably on temperature, meaning that the underlying perturbation of the electronic system is not susceptible to be altered by thermal excitations in the studied temperature range. This finding supports the reasoning put forward in [53] concerning the—absence of—temperature dependence of the proportionality constants scaling the perturbation of the ^{57}Fe hyperfine magnetic field caused by the alteration of the core polarization and that of the conduction electron polarization at iron atoms due to the presence of Co in disordered Fe-Co alloys.

Our results on the present samples thus suggests that the perturbation of the electronic state of iron by the alloying element Co in disordered Fe-Co alloy nanoparticles occurs similarly to that observed in corresponding bulk alloys [28,31,53]. At the same time, correct evaluation of the ^{57}Fe hyperfine magnetic field displayed by Fe-Co alloy nanoparticles

requires the consideration of their nanosized nature and associated collective magnetic excitation effects.

In order to assess the degree of air-stability of the present nanoparticles, an additional Mössbauer-spectroscopy measurement was performed on particles of sample S1 that were directly exposed to ambient air for ~ 4.5 months. The obtained Mössbauer spectrum (Figure S11) reflects the presence of an oxidation product in the form of an associated quadrupole doublet component ($\delta \approx 0.21(1)$ mm/s, $\Delta \approx 0.32(2)$ mm/s) with a relative area fraction of $\sim 13\%$, which may arise from Fe^{3+} ions situated mainly at the tetrahedral site in a $(\text{Fe,Co})_3\text{O}_4$ spinel oxide phase [54,55]. Nevertheless, despite the long-time exposure to air, $\sim 87\%$ of all iron atoms can still be found in the alloy phase, which confirms the considerable stability of the sample under ambient atmospheric conditions.

4. CONCLUSIONS

The applied hydrothermal process leads to bcc $\text{Fe}_x\text{Co}_{1-x}$ alloy nanoparticles that are remarkably stable against oxidation under ambient air, which in practice facilitates their handling and storage in air for suitably long times without substantial degradation. It is demonstrated that the Fe:Co atomic ratio in the samples S1 and S2 ($\sim 53:47$ and $\sim 62:38$, respectively) is consistently revealed by EDX, ICP-MS and ^{57}Fe Mössbauer spectroscopy measurements, provided that the results of EDX are calibrated according to EDX measurements of standard samples. According to the mean ^{57}Fe hyperfine parameters derived from the Mössbauer spectra of S1 and S2 at room temperature the applied preparation method yields alloy samples that are in a fully disordered (A2) atomic state, where the α and β sites of the bcc lattice are taken by iron (or cobalt) in equal proportions. Detailed analysis of the Mössbauer spectra indicate that in these alloys the electronic and spin state of iron atoms is perturbed equally by atoms in their first and second coordination spheres, whereas the effect of atoms in the further atomic shells can be taken into account as an additional broadening of the Mössbauer absorption peaks. Our results regarding the present Fe-Co nanoparticles validate the additivity of the effects of alloying atoms in the first two coordination spheres on the hyperfine magnetic field at the central Fe atom, as well as the absence of appreciable temperature dependence of these effects in the range of 80-293 K.

Acknowledgements

This work was supported by the Hungarian National Research, Development and Innovation Office – NKFIH (K115784 and K115913) and by the Coordenação de Aperfeiçoamento de Pessoal de Nível Superior (CAPES) (Project no. A127/2013).

References

- [1] T. Sourmail, *Prog. Mater. Sci.* **50** (2005) 816-880.
- [2] K.B. Arcuri, L.H. Schwartz, R.D. Piotrowski, J.B. Butts, *J. Catal.* **85** (1984) 349-361.
- [3] P. Rochana, J. Wilcox, *Surf. Sci.* **605** (2011) 681-688.
- [4] K. Schwarz, D.R. Salahub, *Phys. Rev. B* **25** (1982) 3427-3429.
- [5] I. Vincze, I.A. Campbell, A.J. Meyer, *Solid State Commun.* **15** (1974) 1495-1499.
- [6] H.H. Hamdeh, B.Fultz, D.H. Pearson, *Phys. Rev. B* **39** (1989) 11233-11240.
- [7] T. Khmelevska, S. Khmelevskiy, P. Mohn, *J. Appl. Phys.* **103** (2008) 073911 pp. 5.
- [8] B. deMayo, D.W. Forester, S. Spooner, *J. Appl. Phys.* **41** (1970) 1319-1320.
- [9] J.P. Eymery, S.B. Raju, P. Moine, *Phys. Lett.* **68A** (1978) 260-262.
- [10] G.B. Chon, K. Shinoda, S. Suzuki, B. Jeyadevan, *Mater. Trans.* **51** (2010) 707-711.
- [11] A. Hütten, D. Sudfeld, I. Ennen, G. Reiss, K. Wojczykowski, P. Jutzi, *J. Magn. Magn. Mater.* **293** (2005) 93-101.
- [12] A.H. Habib, C.L. Ondeck, P. Chaudhary, M.R. Bockstaller, M.E. McHenry, *J. Appl. Phys.* **103** (2008) 07A307 pp. 3.
- [13] C.S.S.R. Kumar, F. Mohammad, *Adv. Drug Deliver. Rev.* **63** (2011) 789-808.
- [14] W.S. Seo, J.H. Lee, X. Sun, Y. Suzuki, D. Mann, Z. Liu, M. Terashima, P.C. Yang, M.V. McConnell, D.G. Nishimura, H. Dai, *Nat. Mater.* **5** (2006) 971-976.
- [15] S. Xu, A.H. Habib, A.D. Pickel, M.E. McHenry, *Prog. Mater. Sci.* **67** (2015) 95-160.
- [16] H. Moumeni, S. Alleg, J.M. Greneche, *J. Alloy. Comp.* **386** (2005) 12-19.
- [17] D. Kodama, K. Shinoda, K. Sato, Y. Konno, R.J. Joseyphus, K. Motomiya, H. Takahashi, T. Matsumoto, Y. Sato, K. Tohji, B. Jeyadevan, *Adv. Mater.* **18** (2006) 3154-3159.
- [18] K. Zehani, R. Bez, A. Boutahar, E.K. Hlil, H. Lassri, J. Moscovici, N. Mliki, L. Bessais, *J. Alloy. Comp.* **591** (2014) 58-64.
- [19] M. Abbas, Md.N. Islam, B.P. Rao, T. Ogawa, M. Takahashi, C. Kim: *Mater. Lett.* **91** (2013) 326-329.
- [20] D. Carta, G. Mountjoy, M. Gass, G. Navarra, M.F. Casula, A. Corrias, *J. Chem. Phys.* **127** (2007) 204705 pp. 9.
- [21] T.P. Braga, D.F. Dias, M.F. de Sousa, J.M. Soares, J.M. Sasaki, *J. Alloy. Comp.* **622** (2015) 408-417.
- [22] E. Thirumal, D. Prabhu, K. Chattopadhyay, V. Ravichandran, *Phys. Status Solidi A* **207** (2010) 2505-2510.
- [23] J. Kim, J. Kim, J. Kim, K.H. Kim: *J. Appl. Phys.* **113** (2013) 17A313.
- [24] B. Kandapallil, R.E. Colborn, P.J. Bonitatibus, F. Johnson, *J. Magn. Magn. Mater.* **378** (2015) 535-538.

- [25] X.W. Wei, K.L. Wu, G.X. Zhu, Y.J. Liu, W. Shi, X.Z. Li, L.L. Rong, L. Chen, F.H. Wu, *J. Alloy. Comp.* **539** (2012) 21-25.
- [26] M. Alnajjar, D. Quigley, M. Kuntamukkula, F. Simmons, D. Freshwater, S. Bigger, *J. Chem. Health Safe.* **18** (2011) 5-10.
- [27] A. Krietsch, M. Scheid, M. Schmidt, U. Krause, *J. Loss Prev. Process Ind.* **36** (2015) 237-243.
- [28] J.E. Frackowiak, *Phys. Stat. Sol. (a)* **87** (1985) 109-119.
- [29] G.K. Wertheim, V. Jaccarino, J.H. Wernick, D.N.E. Buchanan, *Phys. Rev. Lett.* **12** (1964) 24-27.
- [30] G.K. Wertheim, *Phys. Rev. B* **1** (1970) 1263-1264.
- [31] J.E. Frackowiak, *Hyp. Int.* **60** (1990) 757-760.
- [32] A.W. Burton, K. Ong, T. Rea, I.Y. Chan, *Micropor. Mesopor. Mat.* **117** (2009) 75-90.
- [33] Z. Klencsár, E. Kuzmann, A. Vértes, *J. Radioanal. Nucl. Chem.* **210** (1996) 105-118.
- [34] Z. Klencsár, MossWinn auxiliary DLL library (2015), binary code and source code available for download respectively from http://www.mosswinn.hu/dlls/sub_feco86a.dll and http://www.mosswinn.hu/dlls/sub_feco86a.dpr
- [35] P. Vanysek: Electrochemical Series, in: D.R. Lide (ed.): CRC Handbook of Chemistry and Physics - 87th edition (CRC Press 2006) p. 8-23.
- [36] W. Li, T. Cochell, A. Manthiram: *Sci. Rep.* **3** (2013) 1229-1235.
- [37] I. Ohnuma, H. Enoki, O. Ikeda, R. Kainuma, H. Ohtani, B. Sundman, K. Ishida, *Acta Mater.* **50** (2002) 379-393.
- [38] B. Yang, Y. Cao, L. Zhang, R.F. Li, X.Y. Yang, R.H. Yu, *J. Alloy. Comp.* **615** (2014) 322-326.
- [39] P. Karipoth, A. Thirumurugan, R.J. Joseyphus, *J. Colloid Interface Sci.* **404** (2013) 49-55.
- [40] G. Ouyang, W.G. Zhu, C.Q. Sun, Z.M. Zhu, S.Z. Liao, *Phys. Chem. Chem. Phys.* **12** (2010) 1543-1549.
- [41] Q. Jiang, L.H. Liang, D.S. Zhao: *J. Phys. Chem. B* **105** (2001) 6275-6277.
- [42] X. Zhou, S. Liu, N. Xu, Z. Wu, J. Huang, *Mater. Lett.* **136** (2014) 325-328.
- [43] M. Castrillón, A. Mayoral, A. Urtizbera, C. Marquina, S. Irusta, J.G. Meier, J. Santamaría, *Nanotechnology* **24** (2013) 505702 pp. 11.
- [44] A. Shokuhfar, S.S.S. Afghahi: *Adv. Mater. Sci. Eng.* **2014** (2014) 295390.
- [45] P. Nautiyal, Md.M. Seikh, O.I. Lebedev, A.K. Kundu: *J. Magn. Magn. Mater.* **377** (2015) 402-405.
- [46] S. Mourdikoudis, K. Simeonidis, M. Angelakeris, I. Tsiaoussis, O. Kalogirou, C. Desvaux, C. Amiens, B. Chaudret: *Mod. Phys. Lett. B* **21** (2007) 1161-1168.
- [47] C.W. Chen: Magnetism and metallurgy of soft magnetic materials (Dover Publications: New-York, 1986) p. 320.
- [48] R. Chitrakar, S. Tezuka, A. Sonoda, K. Sakane, K. Ooi, T. Hirotsu, *J. Colloid Interface Sci.* **298** (2006) 602-608.

- [49] W.I.F. David, *J. Appl. Cryst.* **19** (1986) 63-64.
- [50] S. Mørup, *J. Magn. Magn. Mater.* **37** (1983) 39-50.
- [51] B. Fultz, H. Hamdeh, J. Okamoto, *Hyp. Int.* **54** (1990) 799-804.
- [52] M. Rubinstein, *Phys. Rev.* **172** (1968) 277-283.
- [53] H. Hamdeh, J. Okamoto, B. Fultz, *Phys. Rev. B* **42** (1990) 6694-6696.
- [54] P.A. Smith, C.D. Spencer, R.P. Stillwell: *J. Phys. Chem. Solids* **39** (1978) 107-111.
- [55] T.A.S. Ferreira, J.C. Waerenborgh, M.H.R.M. Mendonça, M.R. Nunes, F.M. Costa, *Solid State Sci.* **5** (2003) 383–392.

Table 1. The cubic lattice parameter a , and the characteristic crystallite size, d , derived from XRPD measurements (Figure 1) of the as prepared Fe-Co alloy nanoparticle samples S1 and S2. The fitting error of d is in the order of 0.5 nm.

Sample	a , nm	d , nm
S1	0.28456(1)	24
S2	0.28495(1)	31

Table 2. Fe:Co atomic ratios in samples DS1 and DS2 determined from EDX measurements. The as measured values are the average of 3 successive measurements. These values were corrected on the basis of the calibration curve shown in Figure S1. The statistical uncertainty of the corrected numbers given for DS1 and DS2 is ~ 0.5 and ~ 2 , respectively.

Sample	Fe:Co (as measured)	Fe:Co (corrected)
DS1	70 : 30	53 : 47
DS2	77 : 23	63 : 37

Table 3. Fe:Co atomic ratios in the samples S1 and S2 determined from ICP-MS measurements. The statistical uncertainty of the numbers given for S1 and S2 is ~ 1 and ~ 1.6 , respectively.

Sample	Fe:Co
S1	52 : 48
S2	61 : 39

Table 4. Mean ^{57}Fe hyperfine parameter values of the studied $\text{Fe}_x\text{Co}_{1-x}$ alloy nanoparticles at $T \approx 80$ K and 293 K, as derived from the Mössbauer spectrum fits shown in Figures S7 and S8. δ_m is the mean ^{57}Fe isomer shift relative to $\alpha\text{-Fe}$ at room temperature, whereas $B_{\text{hf},m}$ and $2\varepsilon_m$ denote the mean hyperfine magnetic field and double of the mean first-order quadrupole shift, respectively. Numbers in parentheses denote the statistical uncertainty (standard deviation) in the last digit.

	T , K	δ_m , mm/s	$B_{\text{hf},m}$, T	$2\varepsilon_m$, mm/s
S1	293	0.032(3)	34.43(2)	-0.002(5)
S2	293	0.037(1)	35.38(1)	-0.003(2)
S1	80	0.150(1)	35.38(1)	+0.008(3)
S2	80	0.153(2)	35.86(2)	+0.004(4)

Table 5. ^{57}Fe hyperfine parameters of the studied $\text{Fe}_x\text{Co}_{1-x}$ alloy nanoparticle samples S1 and S2 measured at $T \approx 80$ K and 293 K, as derived from Mössbauer spectrum fits shown in Figure 6. Parameter values denoted with (F) were fixed during the fit. Parameter values common for S1 and S2 were constrained to be equal during the fit. c_{Fe} denotes the concentration of iron in the alloys, RSA stands for the relative spectral area of the magnetic component for which the parameters are given, whereas Γ denotes the common FWHM line width of the Lorentzians the alloy spectrum component model is built up from. Numbers in parentheses denote the statistical uncertainty (standard deviation) in the last digit(s).

	T , K	RSA	δ_0 , mm/s	$\Delta\delta$, mm/s	$B_{\text{hf},0}$, T	ΔB_{hf} , T	$2\varepsilon_0$, mm/s	$\Delta(2\varepsilon)$, mm/s	c_{Fe}	Γ , mm/s
S1	293	94.5(6)	0.015(1)	0.0025(F)	28.69(14)	0.771(6)	0.10(1)	-0.012(1)	0.53(1)	0.294(7)
S2	293	95.4(3)							0.62(1)	0.258(3)
S1	80	97.0(3)	0.139(5)	0.0015(7)	29.66(6)	0.769(8)	0.10(1)	-0.012(1)	0.53(F)	0.368(4)
S2	80	96.4(4)			29.20(7)				0.62(F)	0.334(5)

Figures

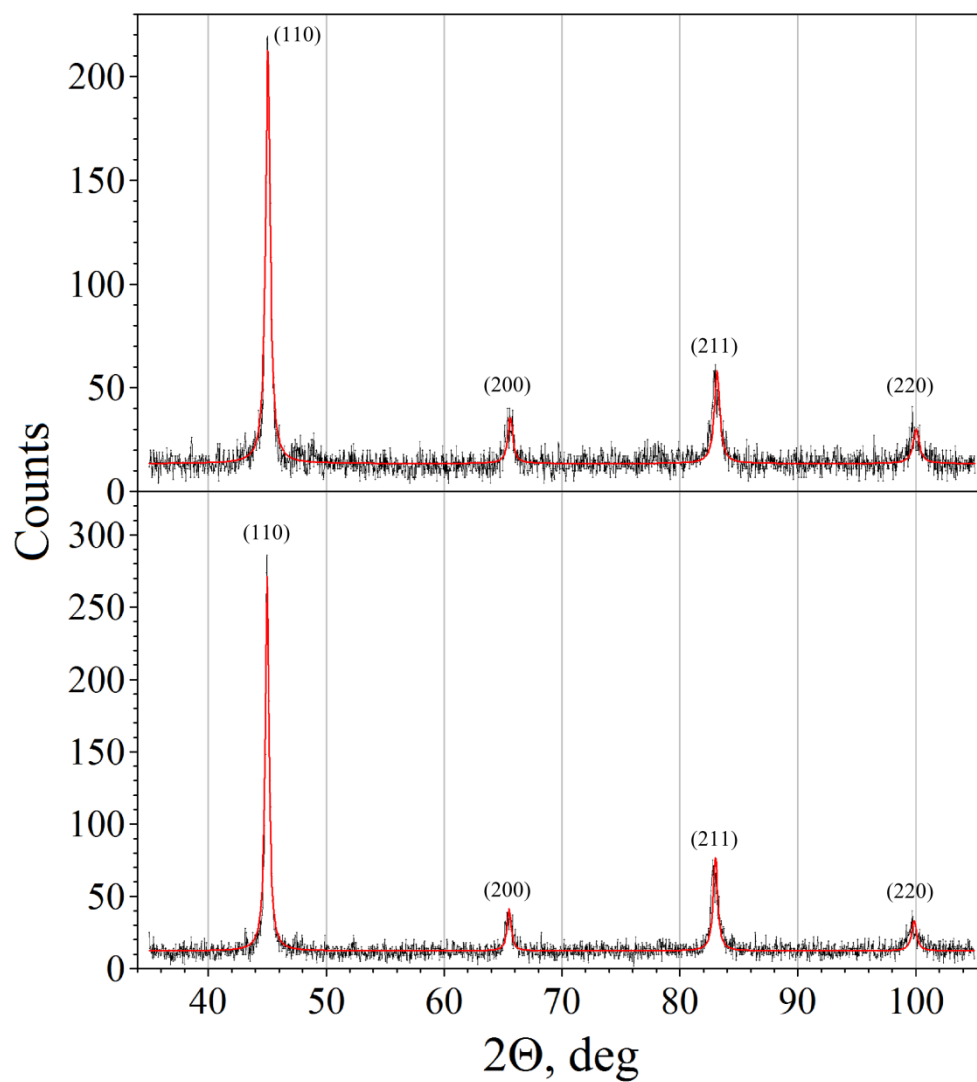


Figure 1. Powder X-ray diffractogram of as prepared alloy samples S1 (top) and S2 (bottom) together with the corresponding fitting curves calculated by assuming a nanocrystalline material having a bcc structure. The corresponding hkl indexes are shown on the top of the peaks.

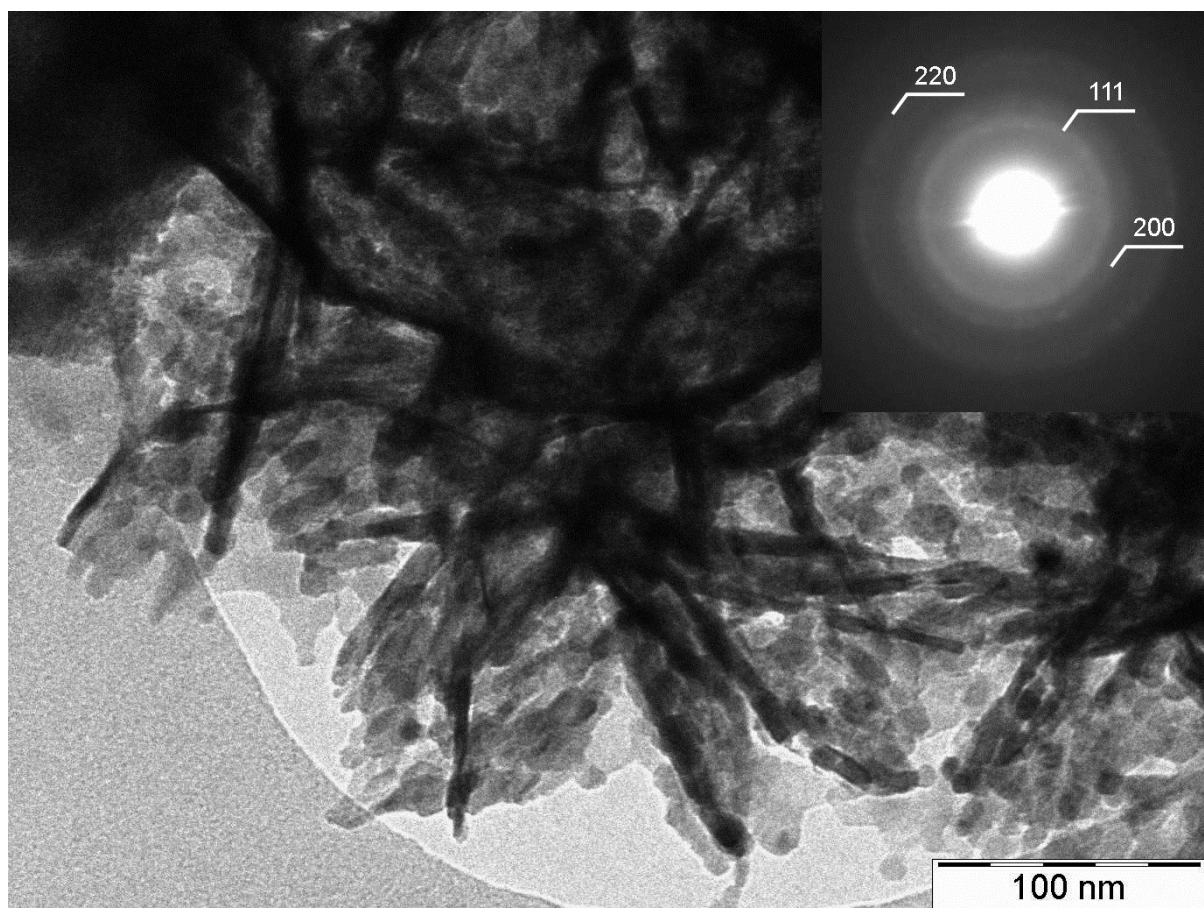


Figure 2. TEM image of the heat treated sample DS1. The inset shows corresponding SAED pattern indexed according to (Co,Fe)O (rock salt structure). See also Figures S2 and S3.

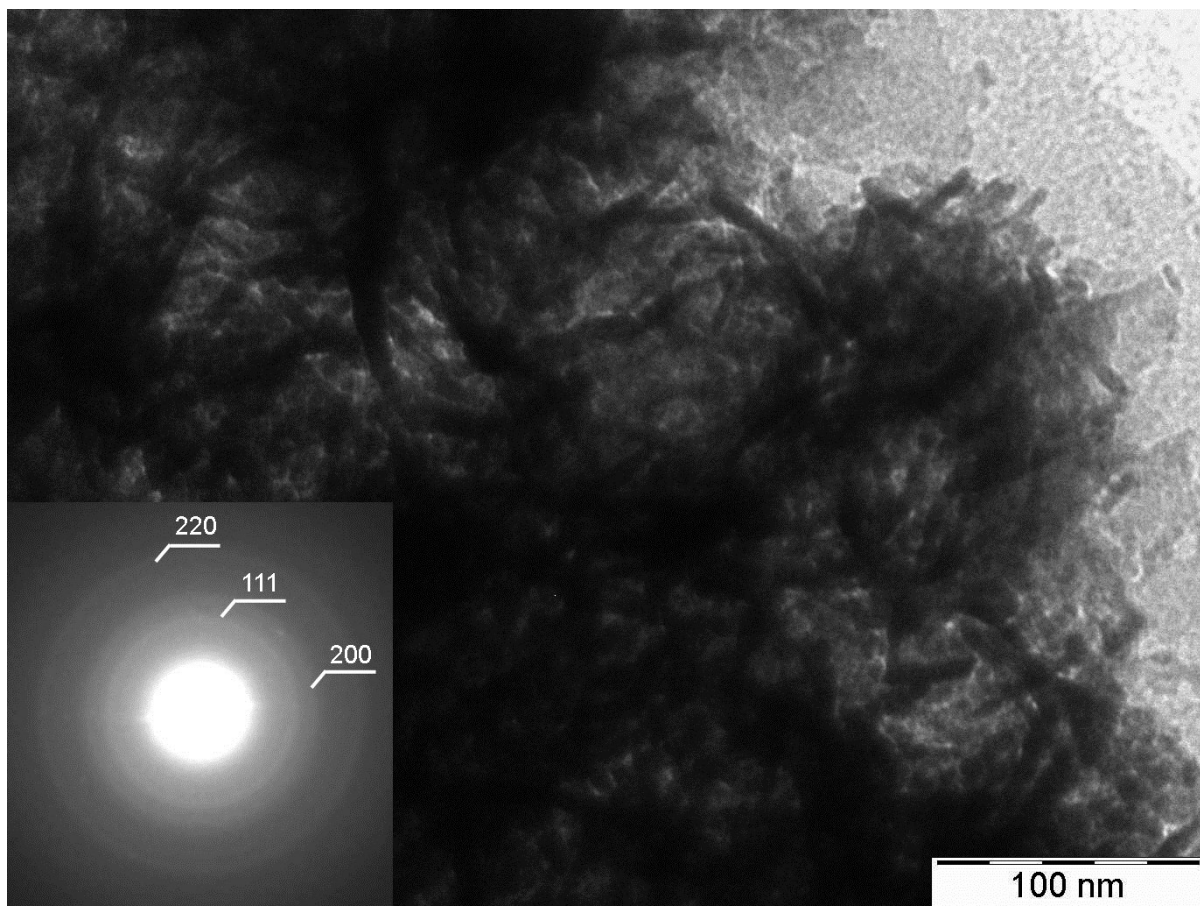


Figure 3. TEM image of the heat treated sample DS2. The inset shows corresponding SAED pattern indexed according to (Co,Fe)O (rock salt structure).

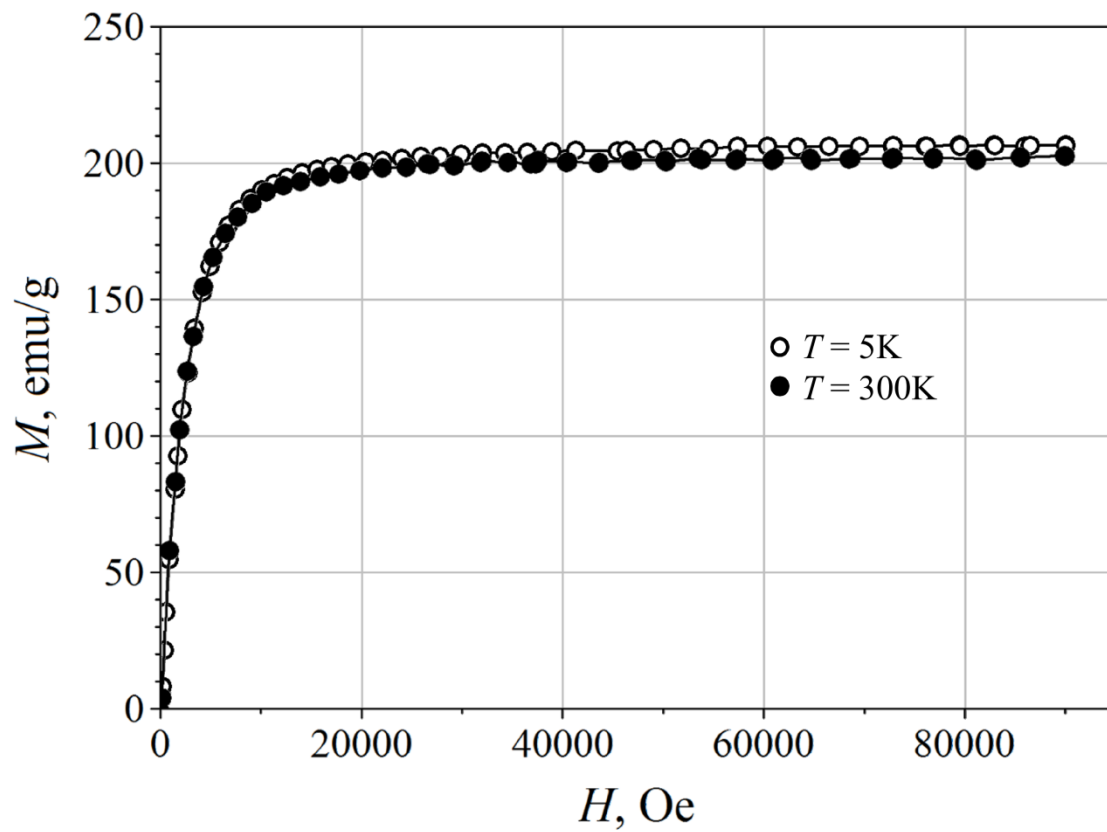


Figure 4. High-field mass magnetization measurements performed on sample S2 at 300 K as well as at 5 K.

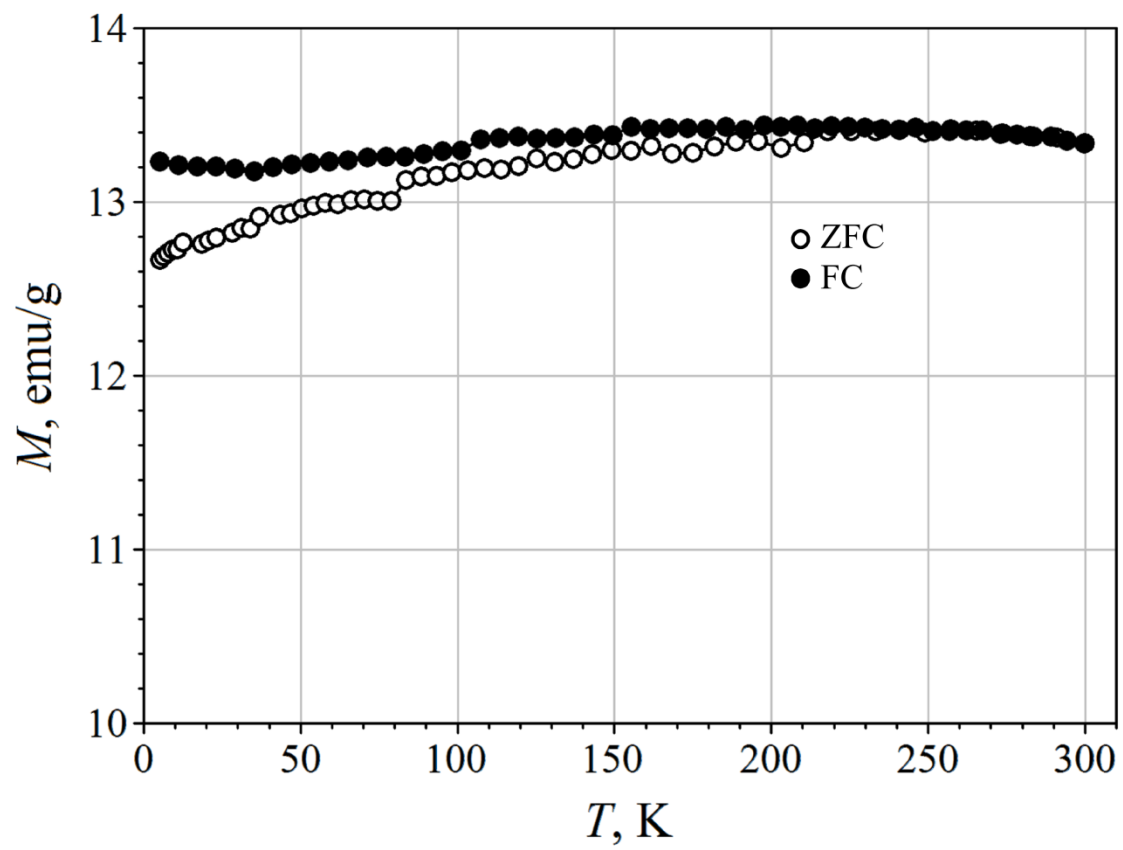


Figure 5. ZFC-FC mass magnetization measurements performed on sample S2 in the temperature range of 5...300 K, by using a driving field amplitude of 118 Oe.

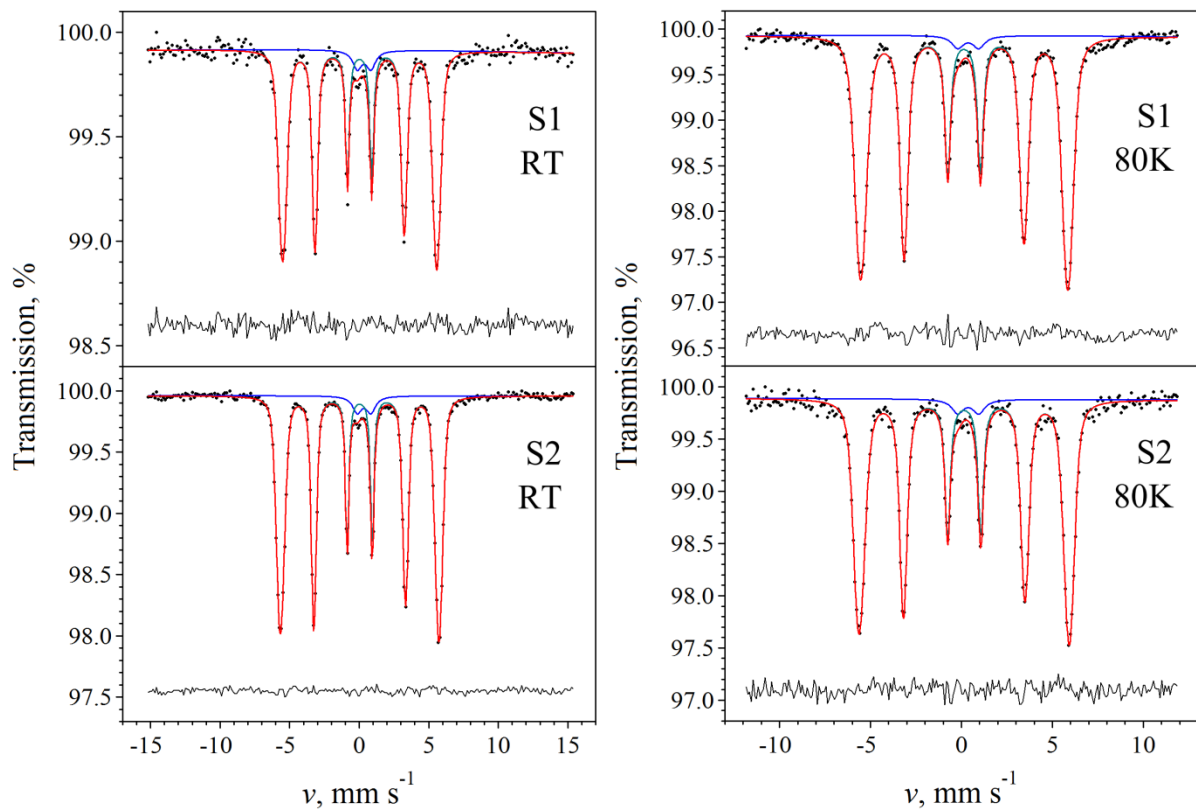


Figure 6. ^{57}Fe Mössbauer spectra (dots) of $\text{Fe}_x\text{Co}_{1-x}$ alloy nanoparticle samples S1 and S2 measured at room temperature ($T \approx 293$ K, left) and at ~ 80 K (right). Solid lines indicate the two subcomponents fitted to the spectra and the corresponding fit envelope. Below the spectra the residual of the fit is displayed. See Table 5 for the resulting fit parameters.